Microporous and Mesoporous Materials 206 (2015) 184–193

Contents lists available at ScienceDirect

Microporous and Mesoporous Materials

journal homepage: www.elsevier.com/locate/micromeso

Novel hierarchically porous nanocomposites of diatomite-based ceramic monoliths coated with silicalite-1 nanoparticles for benzene adsorption

Weiwei Yuan [a,b,c], Peng Yuan [a,c,*], Dong Liu [a,c], Wenbin Yu [a,b,c], Liangliang Deng [a,b,c], Fanrong Chen [a,c]

[a] CAS Key Laboratory of Mineralogy and Metallogeny, Guangzhou Institute of Geochemistry, Chinese Academy of Sciences, Wushan, Guangzhou 510640, China
[b] University of Chinese Academy of Sciences, Beijing 100039, China
[c] Guangdong Provincial Key Laboratory of Mineral Physics and Materials, Wushan, Guangzhou 510640, China

ARTICLE INFO

Article history:
Received 21 October 2014
Received in revised form 2 December 2014
Accepted 3 December 2014
Available online 10 December 2014

Keywords:
Diatomite-based ceramic support
Hierarchically porous nanocomposite
Benzene
Adsorption
Kinetics

ABSTRACT

Novel hierarchically porous nanocomposites of diatomite-based ceramic supports coated with silicalite-1 (Sil-1) nanoparticles for benzene adsorption were prepared via a facile preparation route. In this route, porous ceramic supports with three-dimensional reticulated structures were first prepared using the polymeric sponge method in which diatomite was used as the ceramic framework and polyurethane foam was used as the sacrificial template. This process was followed by facile *in situ* homogeneous coating of Sil-1 on the surface of the ceramic under mild conditions. The hierarchical porosity of the nanocomposites was due to the inherent micropores of Sil-1, the mesopores resulting from the stacking of Sil-1, and the hierarchical macropores of ceramic supports. The specific area and micropore volume of the nanocomposites were 122.9 m^2/g and 0.07 cm^3/g, respectively, with a high zeolite loading of 32.4%. The nanocomposites exhibited a much higher benzene adsorption capacity (133.3 mg/g(Sil-1)) compared with that of a commercial micron-sized ZSM-5 product (66.5 mg/g) and a synthesized Sil-1 (Sil_{SYN}, 94.7 mg/g). Moreover, adsorption–desorption rate constants of the nanocomposites were three and five times higher than those of the ZSM-5 and Sil_{SYN}, respectively, as evaluated via a gravimetric method using an intelligent gravimetric analyzer. The excellent benzene adsorption performance is ascribed not only to the *in situ* silicalite-1 coating process that facilitates the stability and dispersity of Sil-1 on the modified surface of the ceramic supports but also to the hierarchically porous monolithic structure of the nanocomposites, which is beneficial to the mass transfer efficiency for benzene adsorption.

1. Introduction

Silicalite-1, the most well-known aluminum-free MFI-type zeolite, has been extensively used in various industrial fields, such as catalysis, permeation, separation and purification [1–3], in the past two decades. In particular, silicalite-1 nanoparticles (abbreviated as Sil-1 hereafter) exhibit excellent adsorption capacity for volatile organic compounds (VOCs) because of their abundant microporous structures with high specific surface areas [4–7]. Activated carbon is conventionally used as an industrial adsorbent for gases because of its low cost [8,9]. However, poor thermal stability and limited modification flexibility of activated carbon inhibit its application in VOC adsorption. In addition, organic gas molecules adsorbed in the slit-like micropores of activated carbon are difficult to desorb and regenerate [10]. Sil-1 is characterized by high thermal and chemical stability and favorable reusability [11] compared with activated carbon. The regularly straight or zigzag channels of micropores in Sil-1 are advantageous for the desorption of gas molecules [12].

The agglomeration of nanoparticles is well known to lower their effective surface area and reduce their reaction activity, particularly their adsorption performance. Therefore, several methods have been developed to overcome this agglomeration problem [13–17]. Among these methods, the surface modification technique and the loading method have been well established to improve the dispersity of Sil-1. For example, in the surface modification route, Sil-1 was modified by microemulsions [15,18,19] which served as a thermodynamically stable dispersant. The surface of silicalite-1 nuclei were surrounded by nonionic or cationic microemulsions. Thus, the resulting Sil-1 nanoparticles were steadily and uniformly dispersed in the solution because of the strong van der Waals [15] or electrostatic forces [18,19] between the

* Corresponding author at: Guangzhou Institute of Geochemistry, Chinese Academy of Sciences, Wushan, Guangzhou 510640, China. Tel./fax: +86 20 85290341.
E-mail address: yuanpeng@gig.ac.cn (P. Yuan).

http://dx.doi.org/10.1016/j.micromeso.2014.12.004
1387-1811/

microemulsions and the nanoparticles. However, this surface modification route is only applicable in liquid-phase systems, limiting its feasibility in heterogeneous systems. The loading method, in which Sil-1 nanoparticles were coated onto organic or inorganic supports, is an alternative strategy to overcome the agglomeration problem. Non-porous supports such as metals, stainless steel [16,20,21], polymers [22] and inorganic fibers [23,24] have been used to prepare the nanocomposites. However, a drawback of non-porous supports is that the resulting nanocomposites formed from Sil-1 exhibit monomodal microporosity because the pores in Sil-1 are smaller than 1 nm. These structural micropores of silicalite-1 cause diffusion and the related mass transfer limitation of some guest molecules [25]. More recently, substantial efforts have been made to fabricate hierarchically porous Sil-1 nanocomposites. A hierarchically porous nanocomposite structure is capable of increasing the external surface area of Sil-1, shortening the diffusion path and minimizing the diffusion limitations of guest molecules. Assembling Sil-1 nanoparticles on macroporous supports such as porous α-alumina [26,27] enhance the gas adsorption and permeation efficiency of the resulting nanocomposites. However, the low porosity of the porous supports and the high calcination temperature (exceeding 1000 °C) used in their pre-synthesis potentially increases the preparation costs of the nanocomposites. Lu et al. [28] used inexpensive fly ash cenosphere (FAC), which is an aluminosilicate-rich waste produced from power plants, as a support for the coating of Sil-1. However, the readily caused secondary contamination of the FAC support, such as dusting problems, constrains the actual application of the resulting nanocomposites for VOC adsorption. Consequently, identifying desirable porous supports that are environmentally benign and economically viable is important for improving the gas adsorption performance of Sil-1.

Because it is a naturally occurring mineral with well-developed porosity, diatomite is considered as a potential candidate for the synthesis of hierarchically porous nanocomposites [29–32]. Diatomite, also known as diatomaceous earth or kieselgur, is a fossil assemblage of diatom shells. It is characterized by a macroporous structure with pore sizes ranging from the nanometric to micrometric domains [33,34]. Diatom shells are composed of amorphous hydrated silica ($SiO_2{\cdot}nH_2O$) and are classified as opal-A in mineralogy. Because biogenetic mineral aggregates are readily available in ton-scales at low cost and are non-toxic, diatomite has been studied to evaluate its feasibility for use as a support for Sil-1 coating. Wang et al. [35] reported the synthesis of Sil-1/diatomite nanocomposites; they hydrothermally synthesized Sil-1 nanoparticles and assembled them on a modified surface of diatomite using layer-by-layer (abbreviated as LBL hereafter) electrostatic deposition. However, the zeolite loading amount of the resulting nanocomposites was low (10%) because of the weak electrostatic interaction between the nanoparticles and the diatomite. Lu et al. [36] proposed a secondary hydrothermal method for the fabrication of Sil-1/diatomite nanocomposites; in their approach, the hydrothermal growth process was supplemented after the LBL procedure, which resulted in a slightly increased zeolite loading amount (12%). However, the common disadvantages of these two preparation routes are that they require a long synthesis period and need to be conducted under rigorous conditions such as high temperature and high pressure. These disadvantages complicate the preparation and make it less suitable for use in lot-sized production. Clearly, the development of a facile method for coating Sil-1 is needed.

Moreover, in previous studies, the as-synthesized Sil-1/diatomite nanocomposites were in powder form, and their gas adsorption performance was readily disturbed by fluid resistance [35,36]. In particular, the nanocomposites presented a loose two-dimensional (2D) structure and exhibited a low adsorption capacity and low diffusion rate because of the confinement of mass transfer in the 2D space. Mechanically stable monolithic supports with 3D structures, such as porous ceramic supports, have been beneficial in minimizing dusting problems and mass transfer limitations encountered in the gas adsorption process [25,37–39]. Compared with powdered materials, the 3D reticulated structure of the macroporous ceramic monoliths enlarges the contact area between adsorbents and adsorbates, making adsorption and mass transfer of the adsorbates effectively expand to the 3D space and improving the adsorption efficiency of the adsorbents. Among a variety of processing routes [39,40], the polymeric sponge method, also known as the replica technique [39], offers a simple and flexible strategy for the synthesis of macroporous ceramic monoliths. The great versatility of this method is attributed to its simplicity in the fabrication of high-porosity ceramic monoliths and its adaptability to any admirably dispersed ceramic materials. In this sense, testing and verifying the feasibility of using diatomite as a framework material for the preparation of macroporous ceramic monoliths via the polymeric sponge method would be interesting. However, to the best of our knowledge, such studies have not been reported thus far.

In this work, a novel hierarchically porous nanocomposite incorporating advantages from both hierarchically macroporous ceramic supports with unique 3D reticulated structures and a microporous Sil-1 coating was synthesized using a facile method. The simple polymeric sponge method was selected for the fabrication of diatomite-based porous ceramic supports. Then considering that the isoelectric point of SiO_2 is at pH 2 or 3 [41,42], a facile and economic Sil-1 *in situ* coating route on such supports under mild conditions with the aid of electrostatic interaction was adopted instead of the conventional LBL technique or secondary hydrothermal method.

Benzene was used as a model organic compound to evaluate the adsorption performance of the hierarchically porous nanocomposites. Ranked top on the list of VOC pollutants as a human carcinogen, benzene is mainly released from building and decoration materials in indoor environments; it is hazardous to human health and leads to massive acute environmental problems [43–45]. In this work, the benzene adsorption of the novel hierarchically porous nanocomposites was investigated and the structure-adsorption relationship was studied. In particular, an accurate gravimetric method based on the use of an intelligent gravimetric analyzer was applied to assess not only the static adsorption capacity of benzene on the nanocomposites but also the adsorption kinetic parameters [46], which have rarely been reported in previous studies concerning the mechanism of VOC adsorption onto molecular sieves.

2. Experimental section

2.1. Reagents and materials

Tetrapropylammonium hydroxide (TPAOH, 25% aqueous solution, Kente Chemical Co.) and tetraethoxysilane (TEOS, 99%, Aldrich) were used as zeolite synthesis solutions. The ceramic framework material, raw diatomite powder (denoted as Dt), was obtained from the Changbai deposit in Jiling Province, China, and its chemical composition in percent by mass of the respective oxide forms (SiO_2, 86.18; Al_2O_3, 3.08; Fe_2O_3, 1.47; MgO, 0.33; CaO, 0.37; Na_2O, 0.05; K_2O, 0.51; MnO, 0.01; P_2O_5, 0.06; TiO_2, 0.17; and loss on ignition 8.56) was determined by chemical analysis. The ceramic additives were composed of sodium silicate powder (AR grade, Fuchen Reagent Co.) and sodium chloride (AR grade, Sinopharm Reagent Co.). A polyurethane (PU) foam without cell membranes (97% porosity, 50 pores per liner inch) was used as a

sacrificial template and was purchased from Changda Foam Co. Poly(diallyldimethylammonium chloride) (PDDA, 20% aqueous solution, Aldrich) and distilled water (18.2 ΩM cm) were used in all of the experiments. Commercial MFI-type high-silicon molecular sieves (ZSM-5) were purchased from Fuxu Molecular Sieve Co. All of the reagents and materials were used as received, without any further treatment.

2.2. Preparation of diatomite-based porous ceramic supports

Diatomite slurries with 29.3 wt% solid loadings were prepared with a combination of processing additives: 3.0 wt% sodium silicate (binder) and 1.31 wt% sodium chloride (flux) based on the powder content; and 0.76 wt% PDDA (dispersant) based on water content. The slurries were vigorously stirred by a motorized stirrer (700 rpm) for 15 h.

PU foams cut into cubes ($20 \times 20 \times 20$ mm^3) were subsequently immersed into the diatomite slurry under vacuum for 5 min to force the saturated slurry into the foams. The foams were slightly squeezed to remove excess slurry. The immersion process was repeated 5 times to ensure abundant solid loadings. The foams were frozen and dried using a freeze vacuum desiccator to remove the suspension liquid. The green ceramic bodies were slowly heated in air to 600 °C to remove the PU templates and organic additives and were then sintered at 850 °C for 3 h. The resulting diatomite-based porous ceramic supports were denoted as PCS.

2.3. Synthesis of hierarchically porous nanocomposites

A Sil-1 precursor suspension with a molar ratio of 25TEOS:9TPAOH:480H_2O was prepared [47]. The suspension was continuously stirred and aged for 24 h at room temperature and the final Sil-1 precursor suspension presented strong alkaline (pH = 12.5).

Prior to synthesis, 1.5 g of PCS was dipped into 80 ml of 0.5% PDDA solution for 2 h; the PCS was then dried and transferred to the Sil-1 precursor suspension. The suspension with surface-modified supports was treated in a beaker under heating reflux in a silicone oil bath at 101 °C for 72 h. The obtained solid was rinsed with distilled water, calcined at 550 °C for 6 h, and subsequently dried at 80 °C overnight. The resulting sample was denoted as Sil-PCS. Pure Sil-1 without the addition of the supports was also prepared and was denoted as Sil_{SYN}.

2.4. Characterization methods

X-ray diffraction (XRD) patterns were recorded on a Bruker D8 Advance diffractometer at a scan rate of 3° (2θ)/min. The diffractometer was equipped with a Ni filter and a Cu Kα radiation source (λ = 0.154 nm) operated under a generating voltage of 40 kV and a current of 40 mA.

Scanning electron microscopy (SEM) images were obtained using an FEI-quanta 200F field emission scanning electron microscope.

A Micromeritics ASAP 2020 system was used to measure nitrogen adsorption–desorption isotherms at liquid nitrogen temperature (77 K). All of the samples were degassed at 350 °C under vacuum for 12 h before the measurements were performed. The specific area (S_{BET}) was calculated from the nitrogen adsorption data on the basis of the multi-point Brunauer–Emmett–Teller (BET) equation. The micropore volume ($V_{micropore}$) was estimated using the HK method [48]. Micropore and mesopore size distributions in the range of 0.5–20 nm were determined using the non-local density functional theory (NLDFT) model [49,50]. Mercury intrusion tests to determine the macropore size distribution of the samples were conducted on a Micromeritics AutoPore IV 9500 porosimer in the pressure range from 0.1 to 60,000 psi.

Benzene adsorption tests were conducted using an intelligent gravimetric analyzer (IGA-002, Hiden Isochema Instrument) with a sensitivity of 0.1 μg. The samples were pretreated by being heated at 300 °C for 12 h under vacuum to remove the excess water and impurities absorbed onto the surface of the samples. The mass of sample used in each run was approximately 50 mg. Benzene adsorption and desorption isotherms and the equilibrium adsorption capacity were measuring by altering the adsorption and desorption equilibrium pressures. Kinetic constants that reflect the adsorption and mass transfer rate for each pressure increment or decrement were evaluated according to the mass relaxation curves.

3. Results and discussion

3.1. Structural and morphological properties of PCS

As shown in Fig. 1a, the photographs of Dt used as a ceramic framework exhibit a white color in loose powder form. Photographs of the PU foam template and the resulting PCS monolith are displayed in Fig. 1b and c, respectively. The black cubic-shaped PU foam (Fig. 1b) with a side length of 20 mm shows a distinct 3D reticulated macrostructure. The photograph in Fig. 1c shows that the obtained PCS monolith exhibits a cubic shape and a 3D reticulated macrostructure replicated from the PU foam that served as a sacrificial template and that the interconnected open pores of the original template are completely conserved without breaking down during the sintering process. The white color of the resulting PCS monolith, in contrast with the black PU foam template, is ascribed to the removal of the PU foam template and the fabrication of a diatomite-based monolith. The monolith also exhibited slight shrinkage (17 mm), approximately 15% in linear dimensions and 38.6% in volume; this shrinkage is attributed to the dense sintering agglomeration of the diatom powder caused by the binders. The added binders were present in the molten fluid state during the sintering process, which was advantageous for filling the voids of the diatomite particles and for building ceramic monoliths [51]. Then, these fluid-state binders among packed diatomite particles shrunk into a solid state in the subsequent natural cooling process, which led to a slight shrinkage of the resulting dense ceramic monoliths.

As shown in the SEM image (Fig. 1a), the dominant diatom of the Dt sample, classified as the *Coscinodiscus* Ehrenberg (*Centrales*), is disc-shaped and has highly developed macropores with regular pore diameters (0.1–0.8 μm) that vary from the edge of the disc to the center. The diatom frustules are relatively uniform in particle diameter (20–40 μm) and thickness (1.2–1.8 μm). The SEM image in Fig. 1b clearly shows that the PU foam sacrificial scaffolds have a 3D reticulated macrostructure with a pore size in the range of 300–400 μm; the macrostructure is composed of smooth prism struts with a size of approximately 60–70 μm. The SEM images in Fig. 1c show that the as-made PCS monolith possesses a dense 3D reticulated macroporous structure replicated from the PU foam scaffolds after being sintered at 850 °C. The rough prim struts of PCS are composed of sintered particles with diatomite morphology. The macroporous structure of diatomite is clearly observed at a high magnification (Fig. 1c, right). This result is reasonable because the macroporous structure of diatomite is known to remain intact until the calcination temperature is as high as 1100 °C [34]. This characteristic means that PCS possesses a bimodal macroporosity from both the reticulated macroporosity of the PU foam replica and the macroporosity of diatomite.

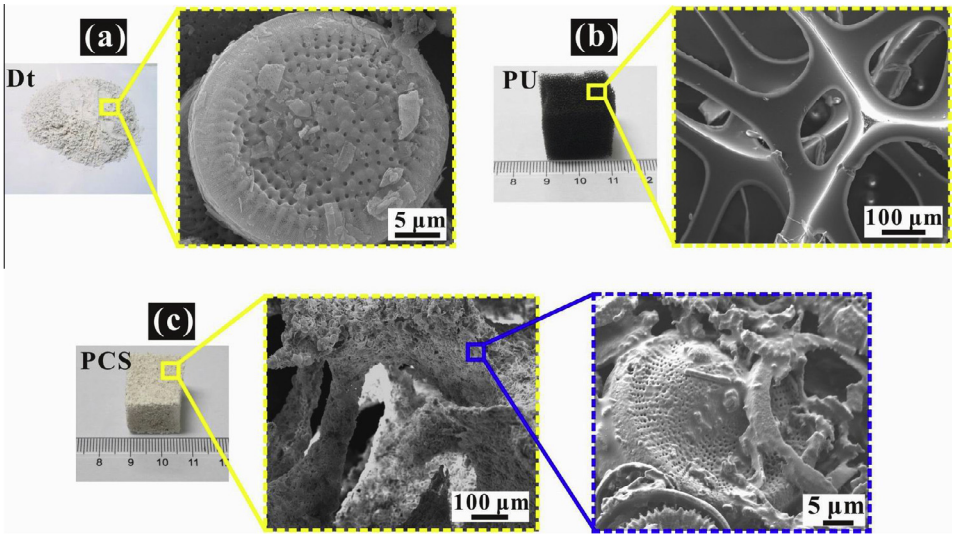

Fig. 1. Photographs and SEM images of (a) Dt, (b) PU foam, and (c) PCS.

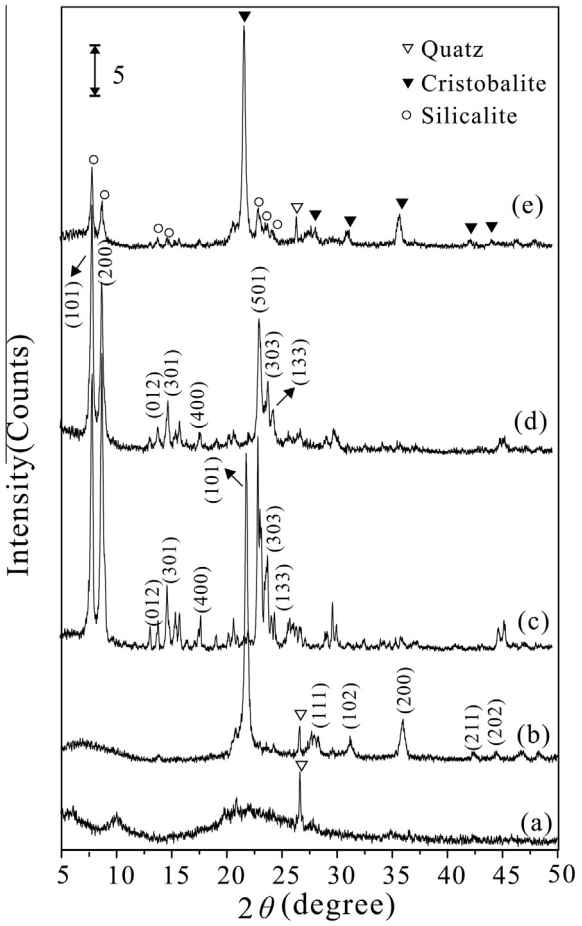

Fig. 2. XRD patterns of (a) Dt, (b) PCS, (c) ZSM-5, (d) Sil_{SYN}, and (e) Sil-PCS.

The XRD pattern of Dt (Fig. 2a) shows a broad peak centered at approximately 21.8°(2θ) with a *d*-spacing of 0.409 nm, which is in agreement with the results for amorphous opal-A reported in the literature [34]. The (101) reflection peak at 26.6°(2θ) indicates the presence of a small amount of quartz impurity in the Dt. The PCS monolith (Fig. 2b) consists mainly of cristobalite (Powder Diffraction File No. 82-0512) according to the newly appeared characteristic peaks at 21.8°, 28.2°, 31.1°, 36.0°, 42.4° and 44.4°(2θ), which are indexed as the (101), (111), (102), (200), (211) and (202) reflections, respectively. This result indicates that the amorphous opal-A silica transformed into cristobalite during the sintering process; however, the macroporous structure of diatomite remained intact, as shown in the SEM image in Fig. 1c. The occurrence of this phase transition is due to the short-range order in the atomic arrangement of opal-A, which is similar to the crystalline structure of cristobalite, favoring the preferential formation of cristobalite during calcination at 850 °C. Thus, the obtained ceramic supports possess significant chemical and thermal stability because of the stable crystalline structure of cristobalite. Notably, in this case, the cristobalite phase appears at a lower temperature than previously reported (above 1000 °C) [52]. This result is attributed to the addition of small amounts of flux, which aided the formation of low-melting-point liquids as binders during calcination. The molten-state active sodium ions present in the liquid binders are characterized by strong diffusion [53], which contributes to defect migration of the diatomite and reduces its phase transition

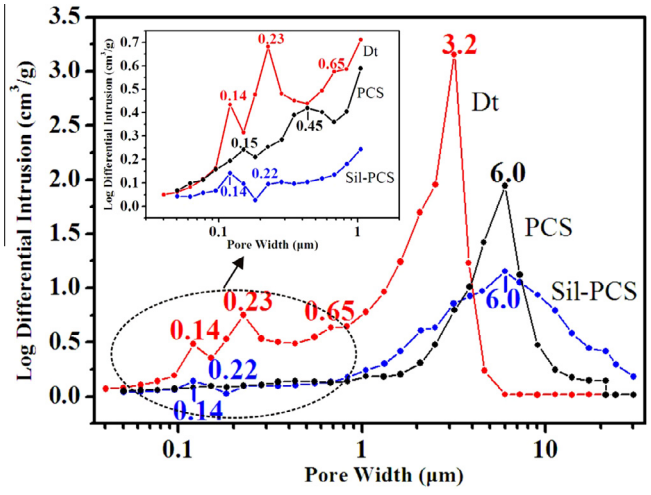

Fig. 3. Macropore size distributions of Dt, PCS and Sil-PCS; inset: magnification of the macropore size distribution (0.01–0.1 μm).

temperature, thereby leading to a stable crystalline silica structure of the resulting PCS monolith.

The macropore size distribution of Dt (Fig. 3), as detected by mercury intrusion tests, clearly exhibits a distinct macropore population centered at approximately 3.2 μm (Fig. 3) and three small populations centered at 0.14, 0.23 and 0.65 μm (insert in Fig. 3). This macropore population and three small populations are attributed to the stacking voids of the diatomite powder particles and the inherent macropores inside the diatomite particles, respectively. In the case of the PCS monolith, the 0.15 and 0.45 μm macropores observed in the inset in Fig. 3 were obtained from the remaining intact macroporous structure of diatomite. This result, in agreement with the SEM observation in Fig. 1c, shows that diatomite macropores remained intact after the samples were sintered at 850 °C. The macropore population of PCS centered at 6.0 μm is attributed to the newly formed stacking voids during the sintering process. The disappearance of the 3.2 μm macropore population in PCS compared with that in Dt is due to the sintering agglomeration of diatomite powder for building the PCS monolith. Additionally, the adhesive disc-shaped particles of the PCS monolith derived from diatomite sintering led to larger stacking void populations centered at 6.0 μm. Unlike the inherent macroporous structure of Dt, the macropore population centers of PCS shifted from 0.65 to 0.45 μm. The reduced populations centered at 0.23 and 0.15 μm are attributed to the blocking of the pores by the fluid-state additives. In addition, the PCS monolith exhibited a high porosity of 65.2%, as evaluated from the mercury intrusion results. This porosity value was higher than that of Dt (57.8%) because of the appearance of ultra-macropore populations centered at 380 μm; these macropores were derived from the replication of the PU foam (see Supplementary Fig. S1).

The nitrogen adsorption–desorption isotherm of Dt (Fig. 4a) is characterized as a type II isotherm with an H3 hysteresis loop [54] according to the International Union of Pure and Applied Chemistry classification. The hysteresis is associated with the filling and emptying of the mesopores by capillary condensation, which implies the existence of a small amount of mesopores in Dt; the presence of these mesopores is consistent with the previous report that diatomite has mesopore sizes that range from 20 to 50 nm [34]. The sharp increase in the nitrogen adsorption at relatively high pressures indicates the existence of macropores in diatomite, which is in agreement with the results of the aforementioned mercury intrusion measurement. The nitrogen adsorption–desorption isotherms of PCS exhibit shapes similar to those of Dt but with less-developed hysteresis loops, indicating that the mesoporosity of PCS was reduced, likely because the fluid-state ceramic additives partly blocked the relatively small diatomite mesopores. As shown in Table 1, the Dt S_{BET} and $V_{micropore}$ values were 24.0 m^2/g and 0.009 cm^3/g, respectively, whereas the corresponding values for PCS were 6.5 m^2/g and 0.003 cm^3/g, respectively (Table 1). The decreased surface area and micropore volume of PCS compared with those of Dt are attributed to the blocking of mesopores and to the reduced stacking voids of PCS resulting from the sintering agglomeration of diatomite particles, as revealed by the mercury intrusion measurement.

3.2. Morphological and textural properties of Sil-PCS nanocomposites

The SEM images in Fig. 5 show the surface morphologies of the Sil-PCS nanocomposites. The synthesized nanocomposites exhibit a 3D reticulated structure with a macropore size of 300–400 μm; as shown in Fig. 5a, this structure resembles that of the PCS monolith. On account of the PCS monolith, which presented cristobalite phase (indicated by Fig. 2b), were not dissolved in the strong alkaline Sil-1 precursor suspension (pH = 12.5), the remained structure of the PCS monolith also implies the high chemical stability of cristobalite in alkaline solution. The prim struts of the Sil-PCS monoliths are composed of adhesive disc-shaped particles with diatomite morphology, as clearly shown in Fig. 5b. The macroporous structure of the diatomite was mostly retained (Fig. 5c) after *in situ* coating of Sil-1 onto the surface of the PCS monoliths. However, the initial smooth surface of diatomite became uneven as the surface was homogenously covered by a layer of spherically shaped Sil-1 with a particle size of approximately 80 nm (Fig. 5c). The homogenous coating of Sil-1 was due to the following mechanism. Considering that the isoelectric point of SiO_2 is at pH 2 or 3 [42], the PCS monolith composed of SiO_2 is negatively charged in the PDDA solution. The electrostatic interaction induced the positively charged PDDA polyions being adsorbed onto the surface of the negatively charged PCS. Thus, the negatively charged amorphous Sil-1 nuclei, which formed under prehydrolysis of the silica source during the aging stage, attached to the surface of the PDDA-modified PCS through electrostatic attraction and the nuclei eventually aggregated into 80 nm crystalline Sil-1 via the *in situ* growth process. This growth mechanism corresponds to the process Tosheva et al. [11] used to synthesize Sil-1, in which Sil-1 nanoparticles were synthesized through aggregation and growth of amorphous nuclei. The spherically shaped, discrete, amorphous Sil-1 nuclei exhibited a particle size in the range of approximately 10–20 nm according to the XRD results (see Supplementary Fig. S2) and SEM images (see Supplementary Fig. S3d).

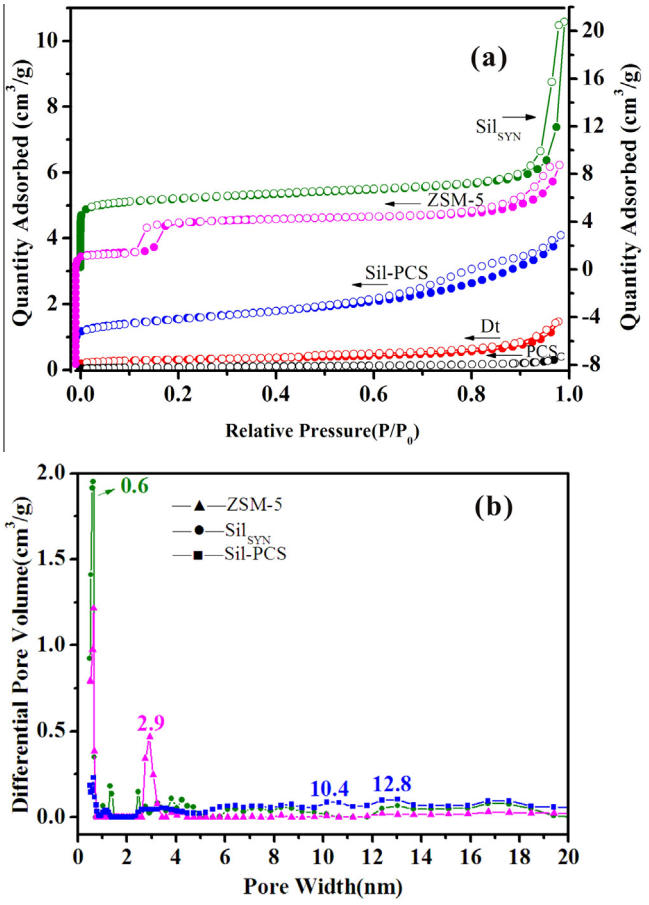

Fig. 4. (a) Nitrogen adsorption (filled symbols) and desorption (open symbols) isotherms of Dt, PCS, ZSM-5, Sil_{SYN} and Sil-PCS. (The arrows indicate the corresponding axes, i.e., the N_2 adsorption quantities of Sil_{SYN} correspond to the right-side vertical axis. And the N_2 adsorption quantities of the others correspond to the left-side vertical axis.) (b) Micropore and mesopore size distributions of ZSM-5, Sil_{SYN} and Sil-PCS.

Table 1
Nitrogen adsorption–desorption results for Dt, PCS, ZSM-5, Sil_{SYN} and Sil-PCS.

Sample	$S_{BET}/m^2\ g^{-1}$	$S_{micropore}$[a]$/m^2\ g^{-1}$	$S_{external}$[a]$/m^2\ g^{-1}$	$V_{micropore}$[b]$/cm^3\ g^{-1}$	$W_{zeolite}$[c] (%)
Dt	24	4.3	20.2	0.009	–
PCS	6.5	2.1	5.0	0.003	–
ZSM-5	330.7	273.7	57.8	0.124	100
Sil_{SYN}	503.3	302.5	207.3	0.196	100
Sil-PCS	122.9	38.1	85.3	0.07	34.2

$W_{zeolite}\% = [V_{micropore}\ (Sil\text{-}PCS) - V_{micropore}(PCS)] \times 100\%/V_{micropore}\ (Sil_{SYN})$.
[a] $S_{micropore}$ was calculated from the *t*-plot surface area, and $S_{external}$ was calculated from the S_{BET} and $S_{micropore}$ using the equation $S_{external} = S_{BET} - S_{micropore}$.
[b] The micropore volume, $V_{micropore}$, was determined using the HK method.
[c] The wt.% of zeolite in Sil-PCS nanocomposites was calculated from the micropore volumes using the equation.

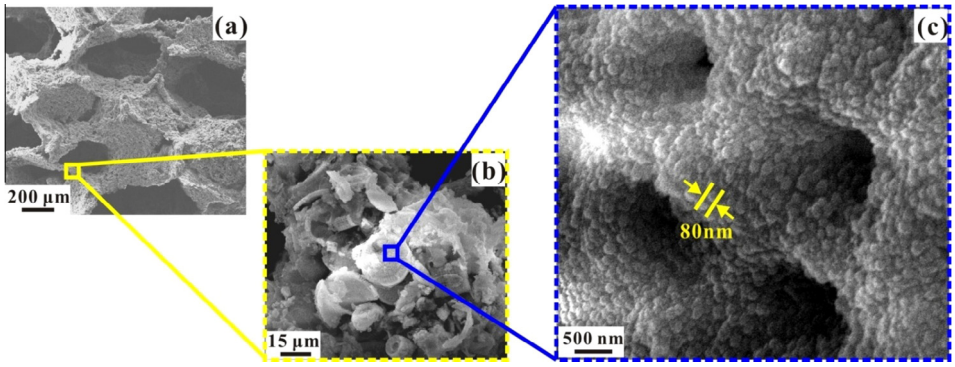

Fig. 5. SEM images of Sil-PCS at various magnifications in (a), (b) and (c).

In previous reports, LBL deposition was employed for the coating of Sil-1 on the surface of diatomite to form Sil-1/diatomite nanocomposites [35,36]. To compare the coating effect between the *in situ* coating process and the conventional LBL deposition technique, a complementary experiment was conducted. The PDDA-modified and negatively charged PCS was placed into suspensions of synthesized Sil-1 with a regular spherical shape with a particle size of 80 nm (see Supplementary Fig. S3a). The surface of PCS was partially covered with a small amount of Sil-1, and large bare areas with no Sil-1 coating were observed (Supplementary Fig. S3b and c). Moreover, the much lower S_{BET} (27.1 m^2/g) of the product compared with that of Sil-PCS (Table 1, 122.9 m^2/g) also suggests that the coating was significantly inhomogeneous. This result indicates that the *in situ* synthesis of Sil-1 on the surface of a PCS monolith described in this work provides an advantage with respect to the homogeneity of the Sil-1 coating compared with the previously reported LBL deposition technique. The reason for this advantage over LBL electrostatic deposition, in which electrostatic attraction occurs between the 80 nm crystalline Sil-1 and the modified support, is the stronger interaction between the smaller Sil-1 nuclei (10–20 nm) and the modified support in the *in situ* coating process. Thus, more nuclei were attracted to the modified surface to achieve an electrical balance, resulting in crystalline Sil-1 grown from the silicalite-1 nuclei that homogenously covered the surface of the PCS monolith.

The XRD patterns in Fig. 2c and d show that both commercial ZSM-5 and Sil_{SYN} exhibit peaks at 7.8°, 8.8°, 13.8°, 14.8°, 17.6°, 23°, 23.6°, 24.4°(2θ), which are indexed as the (101), (200), (012), (301), (400), (501), (303) and (133) reflections of the SiO_2, also called silicalite, according to the Powder Diffraction File No. 44-0696. The adjacent silica tetrahedra of this SiO_2 formed the zig-zag 10-rings channels and the cross-linked straight 10-rings channels through the oxalation [12], possessing the structure of MFI-type zeolite. The XRD pattern of the Sil-PCS nanocomposites in Fig. 2e display peaks of cristobalite at 21.8°, 28.2°, 31.1°, 36.0°, 42.4°(2θ), which are ascribed to the reflections of the PCS monolith (Fig. 2b). Moreover, MFI-type peaks in accordance with those of Sil_{SYN} are also observed in the pattern in Fig. 2e, confirming the coating of Sil-1 on the porous ceramic monoliths. The weaker Sil-1 diffraction intensity of the nanocomposites compared with that of Sil_{SYN} is due to the lower zeolite loading (Table 1) on the surface of the PCS.

The mercury intrusion data (Fig. 3) revealed the macroporous structural changes of the Sil-PCS nanocomposites. A pore population centered at 6 μm forms from the stacking voids of the PCS monoliths, reflecting the remaining intact monolithic framework of the diatomite-based ceramic support. The 0.14 μm macropores of the Sil-PCS nanocomposites shown in the inset of Fig. 3 are ascribed to the preserved macropore structure of diatomite, corresponding to the SEM images in Fig. 5c. However, compared with the pore populations of the PCS monolith, those of the PCS monoliths that were originally centered at approximately 0.45 μm shifted to 0.22 μm. This shift is due to the filling of Sil-1 in the large macropores of the PCS monoliths, which leads to a decrease in pore size for the resulting Sil-PCS nanocomposites.

The nitrogen adsorption isotherms of the Sil-PCS nanocomposites (Fig. 4a) are type IV curves with H3 hysteresis loops. The steep increase in the adsorption amount followed by the mild stage at relatively low pressures ($P/P_0 \leqslant 0.1$) indicates the filling of the Sil-1 micropores, which corresponds to the Sil_{SYN} isotherms. The significant hysteresis loop at $P/P_0 \approx 0.6$ is attributed to the mesopores formed by stacking voids between Sil-1. Compared with the hysteresis loop of Sil_{SYN}, that of the Sil-PCS nanocomposites is formed at a lower pressure ($P/P_0 \approx 0.6$), indicating a more extensive mesopore size distribution than Sil_{SYN}. This result is explained by the unique 3D reticulated monolithic structures of Sil-PCS, which reduced the agglomeration of Sil-1 and increased the likelihood of forming smaller Sil-1 agglomerates; thus, more mesopores were easily formed because of the stacking of smaller agglomerates. The nitrogen adsorption amount of the Sil-PCS nanocomposites increased steadily when P/P_0 approached 1.0, which is in accordance with the slow increase in the amount of micron-sized

ZSM-5 but differs from the steep increase in the adsorption amount of the Sil_{SYN} nanoparticles. This result is attributed to the rapidly increased adsorption amount of the Sil_{SYN} at $P/P_0 \approx 1.0$, which, in turn, is ascribed to the external surface adsorption behavior caused by the agglomeration of Sil-1 [55]. In the case of the Sil-PCS nanocomposites, because the Sil-1 coating process on the surface of PCS reduced their likelihood of agglomeration, the external surface adsorption behavior was alleviated because of the improved dispersity of Sil-1.

The micropore and mesopore size distribution curves of the Sil-PCS nanocomposites calculated via DFT method are shown in Fig. 4b. The major micropore population centered at approximately 0.6 nm is ascribed to the inherent micropores of Sil-1 and is in good agreement with those of ZSM-5 and Sil_{SYN}. The Sil-PCS nanocomposites exhibited mesopore size distributions with pore widths in the range of 2.0–5.0, 6.0–9.0 and 12.0–18.0 nm; these distributions are more extensive than those of ZSM-5 (2.9 nm) and Sil_{SYN} (2.0–5.0 nm). These results are in accordance with the nitrogen adsorption and desorption isotherm results, which show a more significant hysteresis loop in the case of Sil-PCS (Fig. 4a). The intensive mesopore population centered at 2.9 nm for ZSM-5, which is consistent with its small hysteresis loop at $P/P_0 \approx 0.1$ (Fig. 4a), may be related to the industrial synthetic process of the commercial ZSM-5. All of the aforementioned pore size results suggest that these Sil-PCS monolithic nanocomposites characterized by a unique 3D reticulated structure possess hierarchical pores, micropores and stacking mesopores formed from Sil-1 and macropores from Dt and PCS.

The S_{BET} and $V_{micropore}$ values of the Sil-PCS nanocomposites were 122.9 m^2/g and 0.07 cm^3/g, respectively. These values are substantially higher than those of the original Dt and the PCS monolith (Table 1), which is attributed to the introduction of micropores by Sil-1 in the nanocomposites. Because the zeolite loading amount that determines the $V_{micropore}$ values for Sil-PCS is 34.2%, which is lower than the values for ZSM-5 and Sil_{SYN}, the Sil-PCS nanocomposites show a lower $V_{micropore}$ value than the commercial ZSM-5 (0.124 cm^3/g) and Sil_{SYN} (0.196 cm^3/g). This zeolite loading amount of the Sil-PCS nanocomposites is much higher than that of the Sil-1/diatomite nanocomposites (12%) reported by Lu et al. [36], which is attributed to the aforementioned superiority of the *in situ* coating process for Sil-1 over the conventional LBL electrostatic deposition technique. Compared with the conventional LBL deposition technique, the electrostatic attraction in the *in situ* coating process, which could assemble more Sil-1 nuclei on the surface of the modified PCS, offered more growth sites for the Sil-1 nuclei to develop into Sil-1 nanoparticles on the surface of the support. Thus, the Sil-PCS nanocomposites exhibit a higher zeolite loading amount. In addition, compared with the 2D diatomite powder as a support for Sil-1/diatomite nanocomposites, the 3D reticulated PCS support, which largely improves the dispersity of Sil-1, also contributes to the increased zeolite loading amount of the Sil-PCS nanocomposites.

3.3. Performance of Sil-PCS nanocomposites in the benzene adsorption

3.3.1. Benzene adsorption–desorption isotherms

The static adsorption and desorption behaviors of benzene on different samples at 298 K are shown in Fig. 6. Both Dt (Fig. 6a) and PCS (Fig. 6b) show type II adsorption isotherms with very small hysteresis loops. The benzene equilibrium adsorption capacity of PCS (3.0 mg/g (PCS)) is slightly higher than that of Dt (1.0 mg/g(Dt)), although both show a low benzene adsorption capacity. However, the $V_{micropore}$ of PCS (0.003 cm^3/g), which favors the adsorption of benzene molecules, is lower than that of Dt (0.009 cm^3/g), according to the results in Table 1. One reason for this result is that PCS and Dt are mainly composed of macropores

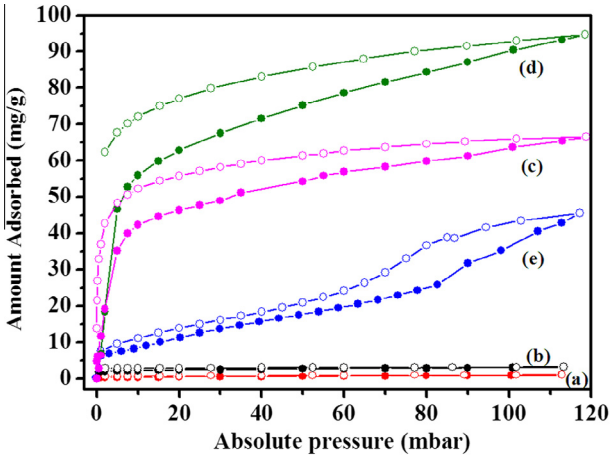

Fig. 6. Benzene adsorption (filled symbols) and desorption (open symbols) isotherms of (a) Dt, (b) PCS, (c) ZSM-5, (d) Sil_{SYN}, and (e) Sil-PCS.

with a very low $V_{micropore}$, which results in low equilibrium adsorption capacities. Another reason is that, in contrast with Dt powder, the 3D reticulated PCS contains channels whose walls are interconnected with each other through the openings. The benzene molecules that enter through the channels of PCS can flow in the 3D direction, increasing the mass transfer rate and the likelihood of collision between benzene and the surface of the adsorbent [37], which is advantageous for the interception of the benzene molecule during the adsorption process. Hence, the 3D reticulated PCS monolith exhibits a slightly higher benzene equilibrium adsorption capacity than the Dt powder in which the mass transfer of benzene molecules only occurs in the 2D direction.

Fig. 6c and d show that both ZSM-5 and Sil_{SYN} exhibit type I adsorption isotherms, which is consistent with the proposal that the type I isotherm is applicable for the adsorption of benzene onto microporous zeolites [56,57]. The initial steep increase in the benzene adsorption at low absolute pressure (5 mbar) indicates the filling of benzene molecular clusters in the micropores, which contributes substantially to the benzene equilibrium adsorption capacity. Additionally, the subsequent increase in benzene adsorption indicates the filling of benzene molecular clusters in the mesopores (2.0–4.0 nm, as indicated by Fig. 4b). The benzene equilibrium adsorption capacities were 66.5 mg/g(Sil-1) for ZSM-5 and 94.7 mg/g(Sil-1) for Sil_{SYN}, which is attributed to their high S_{BET} and $V_{micropore}$ values (Table 1). Sil_{SYN} exhibits a higher benzene adsorption capacity than the micron-sized ZSM-5 because of its higher $V_{micropore}$ (0.196 cm^3/g), which indicates a stronger adsorptive action for benzene [58,59].

The Sil-PCS nanocomposites in Fig. 6e feature typical type IV isotherms with significant hysteresis loops because of the capillary condensation that occurred in mesopores, which resulted from the stacking of Sil-1. The steady increase in the benzene adsorption amount is ascribed to the micropore and mesopore filling process caused by the coating of Sil-1, corresponding to those of ZSM-5 and Sil_{SYN}. Another stage of increased benzene adsorption when the absolutely pressure reaches 80 mbar is attributed to the more extensive mesopore size distribution of the Sil-PCS nanocomposites compared with those of ZSM-5 and Sil_{SYN}. The benzene equilibrium adsorption capacity of the Sil-PCS nanocomposites was 45.6 mg/g(Sil-PCS), substantially exceeding those of Dt and PCS because of the additional micropore and mesopore filling processes. Moreover, the normalized benzene equilibrium adsorption capacity of Sil-PCS was 133.3 mg/g(Sil-1), and the zeolite loading amount of the Sil-PCS nanocomposites was 34.2%, which is higher than that of Sil_{SYN} and ZSM-5. This result is due to the improved dispersity of Sil-1 during the *in situ* coating process and the 3D

reticulated structure of the PCS monolith, which is beneficial to benzene adsorption and mass transfer in its interconnected open pores.

3.3.2. Benzene adsorption–desorption kinetics

The mass relaxation curves for the typical adsorption–desorption steps for benzene (298 K) on ZSM-5, Sil_{SYN} and Sil-PCS nanocomposites, together with the corresponding fit model, are exhibited in Fig. 7. These curves were used to interpret the diffusion mechanism of benzene molecules on various molecular sieve materials, which is critically important for VOC removal in adsorption applications [56]. A linear driving force (LDF) model, which has been successfully used for the adsorption of benzene molecules onto microporous materials such as activated carbon and some mesoporous silica materials [10,56], was used to fit the mass relaxation curve of the samples. In the case of microporous molecular sieves, two diffusion processes are involved in the benzene adsorption dynamics [46]: (a) diffusion through a barrier to enter the pores and (b) diffusion along the pores. The LDF model fits well with the mass relaxation curve when the barrier for entering the pores becomes the rate-determining step for the benzene adsorption process. The LDF model for adsorption is based on the following equation:

$$Mt/Me = 1 - \exp(-kt) \quad (1)$$

where Mt is the uptake at time t, Me is the equilibrium uptake for a given pressure increment, and k is the rate constant. The correspondent LDF model for desorption is based on the equation:

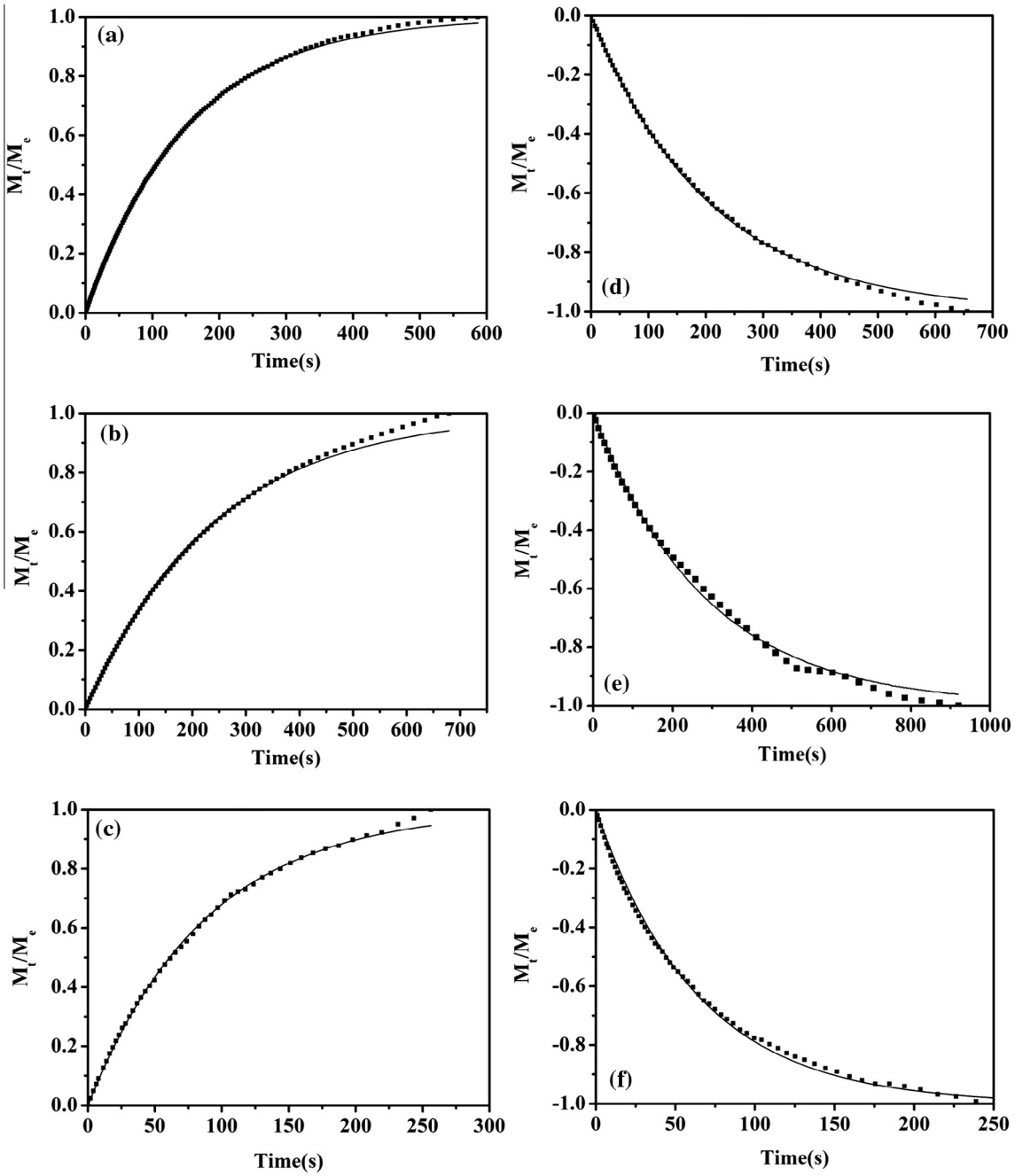

Fig. 7. Variation of Mt/Me vs. time (mass relaxation curves) for adsorption from (a) ZSM-5 (P/P_0 = 0.0588–0.0589), (b) Sil_{SYN} (P/P_0 = 0.0587–0.0591), and (c) Sil-PCS (P/P_0 = 0.0471–0.0473) and desorption from (d) ZSM-5 (P/P_0 = 0.0395–0.0394), (e) Sil_{SYN} (P/P_0 = 0.0591–0.0583), and (f) Sil-PCS (P/P_0 = 0.0792–0.0788).

$$Mt/Me = 1 - \exp(-kt) \quad (2)$$

where Mt is the amount of desorption at time t and Me is the equilibrium amount of desorption for the given pressure decrement.

Fig. 7a–c show the mass relaxation curves of Mt/Me vs. time for the adsorption of benzene onto ZSM-5, Sil_{SYN} and Sil-PCS, respectively. All of the curves fit well with the LDF adsorption model ($R^2 = 0.99$), reaching the criteria for an acceptable fit that almost 99% of residuals should be within the range of ±0.02 [45] (see Supplementary Fig. S4). The curves showing the kinetics of benzene desorption from ZSM-5, Sil_{SYN} and Sil-PCS (Fig. 7d–f, respectively) also fit well with the LDF desorption model ($R^2 = 0.99$), and the residuals are within the range of ±0.02 (Supplementary Fig. S4). This result suggests that benzene diffusion through a barrier to enter the micropores and stacking mesopores of Sil-1 is the rate-determining step for the typical benzene adsorption–desorption process [10]. This barrier may be caused by the similar molecular dynamic diameters of benzene and the micropores of Sil-1 as well as by the external surface diffusion resistance of Sil-1 in the stacking mesopores. The benzene adsorption diffusion time on Sil-PCS (300 s, Fig. 7c) necessary to reach the adsorption equilibrium state was much shorter than those for ZSM-5 (600 s) and Sil_{SYN} (700 s) (Fig. 7a and b), implying that the diffusion of benzene molecules in the Sil-PCS nanocomposites is easier. This result also indicates that the Sil-PCS nanocomposites possess a higher benzene adsorption mass transfer rate than ZSM-5 and Sil_{SYN} at a specific relative pressure ($P/P_0 \approx 0.05$). The Sil-PCS nanocomposites also exhibit corresponding desorption behavior (250 s) superior to that of ZSM-5 (700 s) and Sil_{SYN} (1000 s), which indicates that benzene is more easily removed from the micropores of the nanocomposites in adsorption applications.

Various mass relaxation curves that varied with time were used to obtain different adsorption–desorption kinetic constants for the corresponding relative pressures through LDF model fitting. Fig. 8 shows the variation of the adsorption–desorption rate constants, k, with the variation of relative pressures on ZSM-5 (red symbols), Sil_{SYN} (green symbols) and Sil-PCS (blue symbols). This curve is presented to explain the variation of the benzene molecule diffusion rate in the substantial parts for the entire adsorption-adsorption process, thus helping to assess the potential application feasibility of the synthesized Sil-PCS nanocomposites. In the case of ZSM-5 (red symbols), the adsorption rate constant primarily increases from 0.003 to 0.015 s^{-1} when $P/P_0 < 0.1$ and then decreases to a plateau ($k = 0.005\ s^{-1}$) at $P/P_0 \approx 0.2$. This result can be attributed to the initial monolayer adsorption of benzene followed by the development of benzene molecular clusters in the micropores (0.6 nm) of ZSM-5. The slightly increased adsorption rate constant at $P/P_0 \approx 0.4$ ($k = 0.007\ s^{-1}$) is due to the mesopores filling (2.9 nm) with benzene molecular clusters. The variation of k with the variation of relative pressures on Sil_{SYN} (green symbols) is also shown in Fig. 8. The initial steep increase in the adsorption rate constant ($P/P_0 < 0.1$) from 0.004 to 0.01 s^{-1} is ascribed to the monolayer adsorption of benzene, and the decrease to a plateau ($k = 0.001\ s^{-1}$, $P/P_0 \approx 0.2$) is due to the benzene molecular clustering in the micropores of Sil_{SYN}. The slightly increased rate constant at $P/P_0 \approx 0.25$ (0.003 s^{-1}) is due to a small quantity of mesopores being filled with benzene molecular clusters as a result of the stacking voids of Sil-1. The rate constants exhibit a low value (0.001 s^{-1}) with subtle variation from $P/P_0 \approx 0.3$ to $P/P_0 \approx 1.0$ as a consequence of the monomodal microporosity in Sil_{SYN}. The ZSM-5 exhibits higher rate constants than Sil_{SYN} for the corresponding adsorption increment in the entire adsorption region, which indicates a higher adsorption and mass transfer rate compared with those of Sil_{SYN}. In the case of desorption for both ZSM-5 and Sil_{SYN}, the rate constants are similar to those associated with the adsorption process at the corresponding relative pressures.

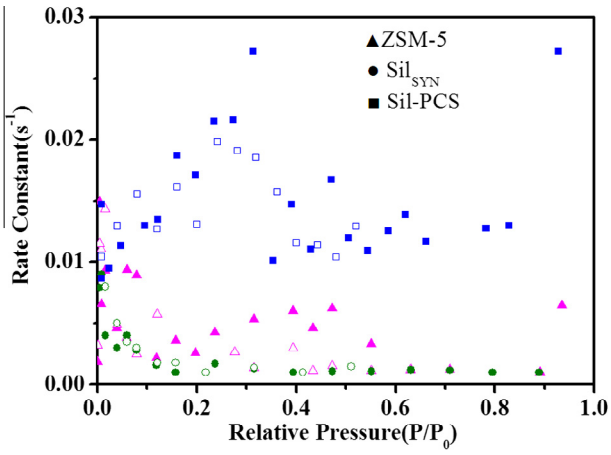

Fig. 8. Rate constant variations for benzene adsorption (filled symbols) and desorption (open symbols) with relative pressure on ZSM-5 (red symbols), Sil_{SYN} (green symbols) and Sil-PCS (blue symbols). (For interpretation of the references to color in this figure legend, the reader is referred to the web version of this article.)

Sil-PCS (Fig. 8, blue symbols) shows a rate constant variation trend that differs significantly from those of ZSM-5 and Sil_{SYN}. The adsorption rate constant gradually increases to a peak ($k = 0.025\ s^{-1}$) without fluctuating until $P/P_0 \approx 0.3$. This behavior is ascribed to the benzene molecular clustering in the inherent micropores and stacking mesopores of Sil-1. This result reflects the fact that the unique 3D reticulated structure of PCS alleviated the agglomeration of Sil-1, thereby improving the Sil-1 dispersity and reducing the likelihood of benzene molecular clustering in the pore walls of Sil-1. Thus, the rate constant steadily increased. The subsequent reduced rate constants for benzene adsorption from $P/P_0 \approx 0.3$ (0.025 s^{-1}) to $P/P_0 \approx 0.8$ (0.013 s^{-1}) is ascribed to the gradually saturated clustering of benzene molecules in the mesopores of Sil-PCS. In the entire adsorption region, Sil-PCS nanocomposites exhibit significantly higher rate constants (0.01–0.025 s^{-1}) for the corresponding adsorption increment than ZSM-5 and Sil_{SYN}. The faster benzene adsorption on Sil-PCS monoliths compared with that on ZSM-5 and Sil_{SYN} powders may be because the benzene molecules that entered through the 3D reticulated structure of the Sil-PCS monoliths can flow in the 3D direction, which facilitates benzene adsorption and the mass transfer process on Sil-PCS. This result also means that these newly synthesized nanocomposites exhibit adsorption and mass transfer behaviors that potentially give them an advantage over ZSM-5 and Sil_{SYN} as the adsorbent in adsorption applications. The desorption rate constants of Sil-PCS exhibit a trend similar to the adsorption rate constants at the corresponding relative pressures. Additionally, the rate constant values of Sil-PCS for the desorption steps (0.01–0.02 s^{-1}) are higher than those of ZSM-5 (0.001–0.015 s^{-1}) and Sil_{SYN} (0.001–0.009 s^{-1}), indicating the potential advantage of Sil-PCS with respect to the removal of molecular benzene from the hierarchical nanocomposites in adsorption applications. The improved adsorption and desorption kinetic performance of the Sil-PCS nanocomposites make them more promising materials in VOC adsorption applications, for example, as an adsorbent in the adsorption rotor [60], compared with the commercial ZSM-5 and Sil_{SYN}.

4. Conclusions

Monolithic nanocomposites of diatomite-based hierarchically macroporous ceramics with microporous Sil-1 coatings for benzene adsorption were prepared. The hierarchically porous

nanocomposites possess 3D reticulated structures with a macroporous structure obtained from the porous ceramic support and microporous and mesoporous structures generated from the inherent pores and stacking voids of MFI-type Sil-1, respectively.

A simple method was used to synthesize hierarchically porous nanocomposites, where a facile *in situ* process for coating MFI-type Sil-1 onto the surface of PDDA-modified diatomite-based ceramic monoliths was conducted for the first time. Sil-1 nanoparticles were homogenously coated onto the surfaces of the ceramic supports, and the obtained nanocomposites possessed a high S_{BET} and $V_{micropore}$, alleviating the agglomeration problem and improving the dispersity and stability of Sil-1.

The synthesized hierarchically porous nanocomposites exhibited excellent benzene adsorption performance, with much higher normalized benzene adsorption capacities than the commercial ZSM-5 and synthesized Sil-1 adsorbents. The adsorption–desorption kinetic equations of the Sil-PCS nanocomposites fit well with the LDF model, indicating that the benzene diffusion through a barrier to enter the micropore and stacking mesopores of Sil-1 is the rate-determining step. The Sil-PCS nanocomposites also display high benzene adsorption–desorption kinetic rate constants, which indicates a superior adsorption and desorption mass transfer rate due to the effective benzene diffusion in the 3D reticulated pore walls of the Sil-PCS monoliths. The benzene adsorption–desorption results demonstrate that the hierarchically porous monoliths are a promising material in VOC adsorption applications.

Acknowledgements

This work was supported by National Key Technology Research and Development Program of the Ministry of Science and Technology of China (Grant No. 2013BAC01B02), Team Project of Natural Science Foundation of Guangdong Province, China (Grant No. S2013030014241), Natural Science Foundation of China (Grant No. 41202024), and the Science and Technology Program of Guangzhou, China. This is a contribution (No. IS-1995) from GIGCAS.

Appendix A. Supplementary data

Supplementary data associated with this article can be found, in the online version, at http://dx.doi.org/10.1016/j.micromeso.2014.12.004.

References

[1] X.J. Zhang, Y. Wang, F. Xin, Appl. Catal. A 307 (2006) 222–230.
[2] J.A. Dunne, R. Mariwals, M. Rao, S. Sircar, R.J. Gorte, A.L. Myers, Langmuir 12 (1996) 5888–5895.
[3] S.K. Wirawan, D. Creaser, Micropor. Mesopor. Mater. 91 (2006) 196–205.
[4] A. Giaya, R.W. Thompson, R. Denkewicz, Micropor. Mesopor. Mater. 40 (2000) 205–218.
[5] L.J. Song, Z.L. Sun, H.Y. Ban, M. Dai, L.V.C. Rees, PCCP 6 (2004) 4722–4731.
[6] M. Yu, J.T. Hunter, J.L. Falconer, R.D. Noble, Micropor. Mesopor. Mater. 96 (2006) 376–385.
[7] Q. Hu, B.J. Dou, H. Tian, J.J. Li, P. Li, Z.P. Hao, Micropor. Mesopor. Mater. 129 (2010) 30–36.
[8] N.J. Foley, K.M. Thomas, P.L. Forshaw, D. Stanton, P.R. Norman, Langmuir 13 (1997) 2083–2089.
[9] A.J. Fletcher, K.M. Thomas, Langmuir 15 (1999) 6908–6914.
[10] B. Dou, J. Li, Y. Wang, H. Wang, C. Ma, Z. Hao, J. Hazard. Mater. 196 (2011) 194–200.
[11] L. Tosheva, V.P. Valtchev, Chem. Mater. 17 (2005) 2494–2513.
[12] R. Krishna, D. Paschek, PCCP 3 (2001) 453–462.
[13] L.H. Wee, L. Tosheva, C. Vasilev, A.M. Doyle, Micropor. Mesopor. Mater. 103 (2007) 296–301.
[14] L. Lakiss, I. Yordanov, G. Majano, T. Metzger, S. Mintova, Thin Solid Films 518 (2010) 2241–2246.
[15] S.J. Lee, D.F. Shantz, Chem. Mater. 17 (2005) 409–417.
[16] S. Mintova, V. Valtchev, V. Engstrom, B.J. Schoeman, J. Sterte, Micropor. Mater. 11 (1997) 149–160.
[17] P. Yuan, M. Fan, D. Yang, H. He, D. Liu, A. Yuan, J. Zhu, T. Chen, J. Hazard. Mater. 166 (2009) 821–829.
[18] S. Axnanda, D.F. Shantz, Micropor. Mesopor. Mater. 84 (2005) 236–246.
[19] S. Lee, D.F. Shantz, Micropor. Mesopor. Mater. 86 (2005) 268–276.
[20] T. Sano, H. Yanagishita, Y. Kiyozumi, F. Mizukami, K. Haraya, J. Membr. Sci. 95 (1994) 221–228.
[21] E. Mateo, R. Lahoz, G.F. de la Fuente, A. Paniagua, J. Coronas, J. Santamaria, Chem. Mater. 16 (2004) 4847–4850.
[22] V. Valtchev, S. Mintova, Micropor. Mesopor. Mater. 43 (2001) 41–49.
[23] V. Valtchev, J. Hedlund, B.J. Schoeman, J. Sterte, S. Mintova, Micropor. Mater. 8 (1997) 93–101.
[24] O. Larlus, V. Valtchev, J. Patarin, A.C. Faust, B. Maquin, Micropor. Mesopor. Mater. 56 (2002) 175–184.
[25] W.C. Li, A.H. Lu, R. Palkovits, W. Schmidt, B. Spliethoff, F. Schuth, JACS 127 (2005) 12595–12600.
[26] X.F. Zhang, H.O. Liu, J.Q. Wang, J. Inorg. Mater. 20 (2005) 947–954.
[27] X.F. Zhang, H.O. Liu, K.L. Yeung, Mater. Chem. Phys. 96 (2006) 42–50.
[28] J. Lu, F. Xu, D. Wang, J. Huang, W. Cai, J. Hazard. Mater. 165 (2009) 120–125.
[29] Z. Cherkezova-Zheleva, M. Shopska, I. Mitov, G. Kadinov, Hyperfine Interact. 198 (2010) 195–210.
[30] X. Liu, C. Yang, Y. Wang, Y. Guo, Y. Guo, G. Lu, Chem. Eng. J. 243 (2014) 192–196.
[31] S. Guo, L. Shi, Catal. Today 212 (2013) 137–141.
[32] Y.J. Wang, Y. Tang, X.D. Wang, A.G. Dong, W. Shan, Z. Gao, Chem. Lett. (2001) 1118–1119.
[33] D. Liu, P. Yuan, D. Tan, H. Liu, M. Fan, A. Yuan, J. Zhu, H. He, Langmuir 26 (2010) 18624–18627.
[34] P. Yuan, D. Liu, D.Y. Tan, K.K. Liu, H.G. Yu, Y.H. Zhong, A.H. Yuan, W.B. Yu, H.P. He, Micropor. Mesopor. Mater. 170 (2013) 9–19.
[35] Y.J. Wang, Y. Tang, A.G. Dong, X.D. Wang, N. Ren, Z. Gao, J. Mater. Chem. 12 (2002) 1812–1818.
[36] J. Lu, F. Xu, W. Cai, Micropor. Mesopor. Mater. 108 (2008) 50–55.
[37] K.S. Yang, J.S. Choi, S.H. Lee, J.S. Chung, Ind. Eng. Chem. Res. 43 (2004) 907–912.
[38] C. Xue, B. Tu, D. Zhao, Adv. Funct. Mater. 18 (2008) 3914–3921.
[39] A.R. Studart, U.T. Gonzenbach, E. Tervoort, L.J. Gauckler, J. Am. Ceram. Soc. 89 (2006) 1771–1789.
[40] T. Ohji, M. Fukushima, Int. Mater. Rev. 57 (2012) 115–131.
[41] G.V. Franks, J. Colloid Interface Sci. 249 (2002) 44–51.
[42] P. He, N. Hu, J.F. Rusling, Langmuir 20 (2004) 722–729.
[43] L. Li, H. Li, X. Zhang, L. Wang, L. Xu, X. Wang, Y. Yu, Y. Zhang, G. Cao, J. Environ. Sci. (China) 26 (2014) 214–223.
[44] L. Huang, J. Mo, J. Sundell, Z. Fan, Y. Zhang, PLoS One 8 (2013).
[45] H. Ahmad Khan, Hum. Exp. Toxicol. 26 (2007) 677–685.
[46] A. Berenguer-Murcia, A.J. Fletcher, J. Garcia-Martinez, D. Cazorla-Amoros, J. Phys. Chem. B 107 (2003) 1012–1020.
[47] P.J. Sterte, L.B. Tosheva, V.P. Valtchev, S.I. Mintova, P.J. Sterte, US Patent 2002/0192155 A1.
[48] G. Horvath, K. Kawazoe, J. Chem. Eng. Jpn. 16 (1983) 470–475.
[49] P.I. Ravikovitch, A.V. Neimark, Langmuir 22 (2006) 10864–10868.
[50] C. Vakifahmetoglu, Ceram. Int. 40 (2014) (1932) 11925–11932.
[51] T.Y. Yang, W.Y. Kim, S.Y. Yoon, H.C. Park, J. Phys. Chem. Solids 71 (2010) 436–439.
[52] P. Yuan, D.Q. Wu, H.P. He, Z.Y. Lin, Appl. Surf. Sci. 227 (2004) 30–39.
[53] W.S. Xiao, W.S. Peng, G.X. Wang, F.Y. Wang, K.N. Weng, Spectrosc. Spectrom. Anal. 24 (2004) 690–693.
[54] P. Yuan, D. Liu, M. Fan, D. Yang, R. Zhu, F. Ge, J. Zhu, H. He, J. Hazard. Mater. 173 (2010) 614–621.
[55] R. Ravishankar, C. Kirschhock, B.J. Schoeman, P. Vanoppen, P.J. Grobet, S. Storck, W.F. Maier, J.A. Martens, F.C. De Schryver, P.A. Jacobs, J. Phys. Chem. B 102 (1998) 2633–2639.
[56] A.J. Fletcher, Y. Yuzak, K.M. Thomas, Carbon 44 (2006) 989–1004.
[57] W. Yu, P. Yuan, D. Liu, L. Deng, W. Yuan, B. Tao, H. Cheng, F. Chen, J. Hazard. Mater. 285 (2015) 173–181.
[58] Y. Yuan, F. Sun, H. Ren, X. Jing, W. Wang, H. Ma, H. Zhao, G. Zhu, J. Mater. Chem. 21 (2011) 13498–13502.
[59] Y. Qin, Z. Mo, W. Yu, S. Dong, L. Duan, X. Gao, L. Song, Appl. Surf. Sci. 292 (2014) 5–15.
[60] H. Yamauchi, A. Kodama, T. Hirose, H. Okano, K.I. Yamada, Ind. Eng. Chem. Res. 46 (2007) 4316–4322.